AIAA JOURNAL
Vol. 45, No. 6, June 2007

Comparison of Time-Domain Impedance Boundary Conditions for Lined Duct Flows

Christoph Richter* and Frank H. Thiele†
Berlin University of Technology, 10623 Berlin, Germany
Xiaodong Li‡
Beihang University, 100083 Beijing, People's Republic of China
and
Mei Zhuang§
Michigan State University, East Lansing, Michigan 48824-1226

DOI: 10.2514/1.24945

Two time-domain impedance models developed recently have been examined and tested numerically. One is based on the three-parameter model of Tam and Auriault augmented by a method to evaluate the effective impedance under flow conditions for a harmonic source. The other is Rienstra's extended Helmholtz resonator model. Its time-domain representation is fully based on the idea of Özyörük and Long to use a z transformation for an impedance function with periodic frequency response. The implementation of the models in a numerical simulation tool with the dispersion relation preserving scheme is discussed in detail. A filtering approach guarantees the stability of the Myers boundary condition. The results from both of the two models agree notably well with each other. The validation and verification of both models are carried out for the latest NASA impedance tube experiment. The adaptability to realistic inlet configurations is shown using a generic aeroengine geometry with available numerical results. Overall, both models give a similar physical behavior if limitations are carefully considered. The extended Helmholtz resonator is used as termination impedance. A broadband impedance eduction is successfully carried out, resulting in an extended Helmholtz resonator representation for a ceramic tubular liner.

Nomenclature

$\underline{A}, \underline{B}, \underline{C}, \underline{D}$	=	coefficient matrices (LEE)
$\boldsymbol{F}(\phi')$	=	flux vector (LEE)
i	=	imaginary unit, $e^{i\omega t}$ convention
m	=	face reactance (EHR)
n	=	radial mode number
$\boldsymbol{n}$	=	wall normal vector
p	=	pressure amplitude
p'	=	pressure perturbation
p_0	=	mean pressure
R	=	face resistance (EHR)
R'_0	=	effective resistance parameter (EFI)
s_p	=	auxiliary variable (EFI and EHR)
T_l	=	period time (EHR)
u_n	=	normal velocity amplitude
$\boldsymbol{u}_0$	=	mean velocity vector
u'_n	=	normal velocity perturbation
$\boldsymbol{u}'$	=	velocity perturbation
X'_{+1}	=	effective reactance parameter (EFI)
X'_{-1}	=	effective reactance parameter (EFI)
Z	=	complex impedance
β	=	cavity reactance (EHR)
γ	=	ratio of the specific heats
ε	=	cavity resistance (EHR)
κ	=	correction coefficient (EFI and EHR)
$\mu(t)$	=	Myers term (EHR)
ν	=	azimuthal mode number
σ_x	=	damping coefficient
ϕ'	=	perturbation state vector
ω	=	angular frequency
ϱ_0	=	mean density
ϱ'	=	density perturbation

Presented as Paper 2527 at the 12th AIAA/CEAS Aeroacoustics Conference (27th AIAA Aeroacoustics Conference), Cambridge, MA, 8–10 May 2006; received 3 May 2006; revision received 24 August 2006; accepted for publication 14 February 2007.

*Graduate Engineer, Institute of Fluid Mechanics and Engineering Acoustics, Müller-Breslau-Strasse 8; richter@cfd.tu-berlin.de.

†Professor, Institute of Fluid Mechanics and Engineering Acoustics, Müller-Breslau-Strasse 8; frank.thiele@cfd.tu-berlin.de.

‡Professor, School of Jet Propulsion, Xueyuan Road 37; lixd@buaa.edu.cn.

§Associate Professor, College of Engineering, 2448 Engineering; zhuangm@msu.edu.

I. Introduction

AEROENGINE noise reduction is, in today's turbine design, achieved principally by using passive-acoustic treatments. Reductions of noise in the forward arc of aeroengines are achieved by acoustic lining of the nacelle interior. The same method also provides an essential technique to reduce the core noise and the fan noise propagating to the backward arc of aeroengines.

For many applications, a description of the acoustic lining in the frequency domain is sufficient. However, a description in the time domain is highly desired when dealing with multifrequency and broadband acoustic sources or nonlinear phenomena. The time-domain methods could expand the capability and reduce the turnaround time of the aeroengine design in these cases. Prospectively broad applicable time-domain impedance boundary conditions could expand the choice of boundary conditions for highly accurate computational aeroacoustics (CAA) and computational fluid dynamics (CFD) simulations by the possibility to use measured impedance values.

The description of a locally reacting surface by a complex impedance $Z(i\omega)$ for each frequency is a standard technique in acoustics. A time-domain representation of this definition contains a convolution integral in general. The impedance is initially defined without a flow on the surface. To extend the impedance condition for surfaces with subsonic flow the conservation of the continuity of

particle displacement over an assumed infinite thin shear layer [1,2] is required, unless the boundary layer on the impedance surface is resolved. The direct, time-domain representation of this model is physically unstable [3,4]. The design of a time-domain impedance boundary condition must address both of the aforementioned problems. There were different successful attempts to develop and apply time-domain impedance models for specific problems in the past [4–8]. However, because all authors report some drawbacks or limitations, the choice remains open when looking for a reliable method with application to realistic problems.

There have been some promising new achievements in time-domain impedance modeling for subsonic flows that motivated the current study. The aim of this paper is to compare two different time-domain impedance boundary conditions representing the current state of the art. One is the effective impedance model (EFI) of Li et al. [9]. It goes back to the ideas of Tam and Auriault [4] and is explicitly designed for the application with a CAA method. On the other hand, there is a promising class of models based on the idea of Özyörük and Long [5] to use a technique known from electromagnetism as z transform. A new theoretical assessment was given by Rienstra [10]. It distinguishes the model for the frequency response of the impedance and its time-domain representation based on a z transformation clearly from the numerical method. This work prepared the way for an application of z-transform-based, time-domain impedance models with arbitrary numerical methods [11,12].

The focus of the current study are the accuracy and time requirements with respect to a possible application of the models in nacelle-liner design. The application of a broadband impedance model as termination impedance is also successfully demonstrated using a measured impedance for the nonperfect, nonreflective, throughflown termination of a duct. The broadband parameter eduction to fit experimental data by one impedance model with broadband capabilities is also successfully demonstrated in this paper.

The paper is organized as follows: In Sec. II the mathematical model and the numerical method to simulate the wave propagation in a ducted environment are summarized. In Sec. III the mathematical backgrounds of the two different time-domain impedance models developed recently, EFI and extended Helmholtz resonator (EHR), are given. In Sec. IV, numerical results of both models are discussed and compared with each other and to the experimental and numerical results from the literature [13–15]. The conclusions are drawn in Sec. V.

II. Mathematical Model and Numerical Method

The governing equations describing the propagation of small perturbations moving fluid are the linearized Euler equations (LEE)

$$\frac{\mathrm{D}\varrho'}{\mathrm{D}t} + \boldsymbol{u}' \cdot \nabla \varrho_0 + \varrho_0 \nabla \cdot \boldsymbol{u}' + \varrho' \nabla \cdot \boldsymbol{u}_0 = 0 \tag{1}$$

$$\frac{\mathrm{D}\boldsymbol{u}'}{\mathrm{D}t} + \frac{\varrho'}{\varrho_0}\boldsymbol{u}_0 \cdot \nabla \boldsymbol{u}_0 + \boldsymbol{u}' \cdot \nabla \boldsymbol{u}_0 + \frac{1}{\varrho_0}\nabla p' = 0 \tag{2}$$

$$\frac{\mathrm{D}p'}{\mathrm{D}t} + \gamma p_0 \nabla \cdot \boldsymbol{u}' + \left(\boldsymbol{u}' - \frac{p'}{p_0}\boldsymbol{u}_0\right) \cdot \nabla p_0 = 0 \tag{3}$$

The linearized material derivative, for example, of the pressure perturbation is defined as follows:

$$\frac{\mathrm{D}p'}{\mathrm{D}t} = \frac{\partial p'}{\partial t} + \boldsymbol{u}_0 \cdot \nabla(p')$$

The preceding system of equations describes not only the acoustic wave propagation but also the propagation of vorticity and entropy waves; it is therefore not fully equivalent to the wave equation of the acoustic potential used by most of the frequency-domain methods.

Only axisymmetric and 2-D problems are addressed by the current study. The nabla operator in 2-D for the coordinate system (x, y) and the basis vectors $\boldsymbol{e}_x$ and $\boldsymbol{e}_y$ is given by

$$\nabla_{\mathrm{2D}} = \frac{\partial}{\partial x}\boldsymbol{e}_x + \frac{\partial}{\partial y}\boldsymbol{e}_y$$

In case of axisymmetric boundary and mean-flow conditions the nabla operator is defined as follows:

$$\nabla_{\mathrm{Axi}} = \frac{\partial}{\partial x}\boldsymbol{e}_x + \frac{\partial}{\partial r}\boldsymbol{e}_r - \frac{im}{r}\boldsymbol{e}_\varphi$$

assuming a $e^{i\omega t}$ convention throughout the paper. In this case the derivatives of the basis vectors $\boldsymbol{e}_r$ and $\boldsymbol{e}_\varphi$ have to be considered. The azimuthal derivative of the perturbations is replaced by the preceding modal approach and the mean flow is considered constant ($m = 0$) in φ direction [16]. The system is written in matrix-vector form, for example, for an axisymmetric case

$$\frac{\partial \phi'}{\partial t} = -\underline{A} \cdot \frac{\partial \phi'}{\partial x} - \underline{B} \cdot \frac{\partial \phi'}{\partial r} - \frac{1}{r}\underline{C} \cdot \phi' - \underline{D} \cdot \phi' = \boldsymbol{F}(\phi') \tag{4}$$

For a 2-D, rectangular geometry r is replaced by y and the matrix $\underline{C}$ equals zero, whereas $\underline{A}$, $\underline{B}$, and $\underline{D}$ remain unchanged.

The numerical method is based on the fourth-order dispersion relation preserving (DRP) scheme [17] for the spatial discretization. At the boundaries such as the walls and open ends of a duct, optimized backward stencils of fourth and third order are used. The time marching is performed by the alternating five/six-stage low dissipation, low dispersion Runge–Kutta (LDDRK) method [18] implemented in 2N storage form [19]. An 11-point-stencil central Taylor filter (FIR) of the tenth order is used to eliminate parasite waves [20]. At the boundaries, central filters of lower orders are applied.

The nonreflective boundary condition for duct open ends is based on the perfectly matched layer (PML) [21]. The PML equations can be written as follows for a layer added in x direction with the 1-D mean-flow Mach number M_x:

$$\frac{\partial \phi'}{\partial t} = \boldsymbol{F}(\phi') - \sigma_x \phi' - \sigma_x \underline{A} \cdot \frac{\partial \phi'_1}{\partial r} - \frac{M_x}{1 - M_x^2}\sigma_x \underline{A} \cdot \phi' \tag{5}$$

where ϕ'_1 denotes the auxiliary vector defined by $\dot{\phi}'_1 = \phi'$ and $\boldsymbol{F}(\phi')$ is an abbreviation for the right-hand side of Eq. (4). The last term was obtained by Hu [21] from a Prandtl–Glauert transform to ensure that the PML remains well-posed under homogeneous mean-flow conditions. The PML coefficient σ_x is increased in a zone of about 20 grid points towards the outer boundary at an open end. As actual boundary condition the outermost grid line is set to zero for all perturbation components.

A simple sponge layer that adds damping is used at the boundary with an incoming sound source

$$\frac{\partial \phi'}{\partial t} = \boldsymbol{F}(\phi') - \sigma_x(\phi' - \phi'_{\mathrm{source}}) \tag{6}$$

The sound source defined by ϕ'_{source} is harmonic for most of the cases and a multifrequency periodic perturbation for the global impedance eduction. The spatial shape of ϕ'_{source} is always chosen to represent single duct modes. The outermost three grid lines of the source are given by a Dirichlet boundary condition.

For the axisymmetric cases, a modal symmetry boundary condition with a singularity treatment is used at the axis [16]. The boundary conditions of impedance walls and hard walls as a main focus of this paper are discussed in the following section.

III. Time-Domain Impedance Models

This section consists of the following basic parts: In Sec. III.A wall boundary conditions [22] for the DRP [17,23] are briefly described to prepare for the introduction of the impedance boundary conditions, whereas Sec. III.B discusses the influence of a mean flow on the

impedance following Myers [2]; in Secs. III.C and III.D the two time-domain impedance models EFI [4,9] and EHR [5,10] are presented, respectively.

A. Wall Boundary Conditions for Computational Aeroacoustics

The wall boundary condition for CAA methods is usually stated in terms of a condition to the normal velocity $u'_n(t)$ at a given time. The mathematical model to describe the sound propagation is based on the LEE here; it could also be based on the nonlinear Euler equations. All these models contain a form of the momentum equation that connects $\dot{\boldsymbol{u}}'(t)$ to the pressure gradient. The momentum equation Eq. (2) can be expressed as follows:

$$\frac{\partial \boldsymbol{u}'}{\partial t} = \boldsymbol{f}(\varrho_0, \boldsymbol{u}_0, \varrho', \boldsymbol{u}', \ldots) - \frac{1}{\varrho_0}\nabla p' \tag{7}$$

Taking the scalar product with the unit normal vector of a resting wall surface this equations reads

$$\frac{\partial u'_n}{\partial t} = f_n(\varrho_0, \boldsymbol{u}_0, \varrho', \boldsymbol{u}', \ldots) - \frac{1}{\varrho_0}\mathbf{n}\cdot\nabla p' \tag{8}$$

where the subscript n denotes the normal component of a vector. It is important to note that the pressure is not present in f_n and $\boldsymbol{f}$.

Tam and Dong [22] showed that the discretized system obtained by the application of the DRP scheme does not allow additional boundary conditions at a wall. Their solution is to introduce an additional degree of freedom for each additional condition to the discretized system. Tam and Dong implemented this degree of freedom by introducing ghost points adjacent to the wall but outside the computational domain. If the time derivative of the normal velocity at the surface $\dot{u}'_n$ is provided by the time-domain impedance model, the ghost-point pressure can be calculated from Eq. (8). The discretized system provides f_n without the information from the ghost point. A detailed discussion of the implementation is presented by Li et al. [9].

B. Mean-Flow Effect on a Linear Liner

The complex impedance of a lined wall is defined as a function of frequency

$$Z(i\omega) = \frac{\tilde{p}(i\omega)}{\tilde{u}_n(i\omega)} \tag{9}$$

where $\tilde{u}_n(i\omega)$ and $\tilde{p}(i\omega)$ are the complex amplitudes directly at the impedance surface outside the flow. To formulate the impedance definition that allows a flow adjacent to the locally reacting impedance surface, Myers [2] assumes a continuity of the particle displacement over an infinite thin shear layer. The consideration of a particle continually moving over the shear layer leads to a connection of $\tilde{p}$ and $\tilde{u}_n$ to the perturbations at the surface but inside the steady moving fluid denoted by p and u_n. A schematic of a cavity-type liner given in Fig. 1 shows both a nonslip and a slip mean-flow condition. In terms of the complex amplitudes of p and u_n in the frequency domain, the impedance boundary condition of Myers is written as

$$u_n(i\omega) = \frac{p(i\omega)}{Z(i\omega)} \underbrace{+\boldsymbol{u}_0\cdot\nabla\left(\frac{p(i\omega)}{i\omega Z(i\omega)}\right)}_{\text{convective term}} \underbrace{-\frac{p(i\omega)}{i\omega Z(i\omega)}\boldsymbol{n}\cdot(\boldsymbol{n}\cdot\nabla\boldsymbol{u}_0)}_{\text{curvature term}} \tag{10}$$

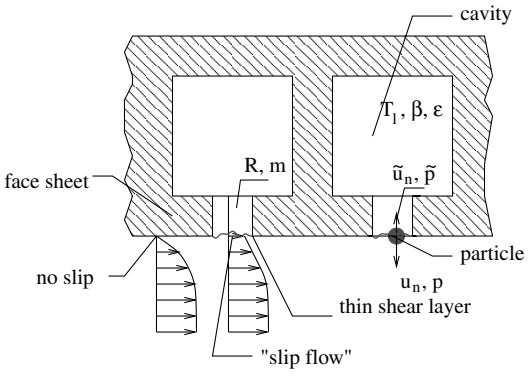

Fig. 1 Scheme of a liner.

Different from the preceding section, the direction of the normal vector has to be specified now; $\boldsymbol{n}$ is defined as positive when pointing into the impedance surface. The additional terms of Eq. (10), when compared to Eq. (9), show the effects of the convection with the mean flow and the curvature of the impedance surface. As can be seen, these two terms become zero without a mean flow ($\boldsymbol{u}_0 = \boldsymbol{0}$). In this case Eq. (10) returns to Eq. (9) as the assumed thin shear layer vanishes and the field variables on both sides are equal. Numerical results of Zhuang [24] have shown that the solution of a nonslip mean flow with vanishing boundary layer thickness converges to the solution of the respective slip mean flow based on the assumption of the continuity of particle displacement.

C. Effective Impedance Model

The three-parameter broadband time-domain impedance boundary condition by Tam and Auriault [4] can be extended for subsonic mean flows and written as

$$\frac{\partial p'}{\partial t} = R'_0\frac{\partial u'_n}{\partial t} - X'_{-1}u'_n + X'_{+1}\frac{\partial^2 u'_n}{\partial t^2} \tag{11}$$

This model can be seen as a mass-spring-damper representation for the frequency response of the effective impedance. It is equivalent to a frequency-domain impedance boundary condition defined with the effective impedance Z' by

$$Z' = R'_0 + i[X'_{-1}/\omega + X'_{+1}\omega] \tag{12}$$

The requirement of a passive impedance and the analysis of stability and well posedness [4,9] provide the limits for the three parameters as $R'_0 > 0$, $X'_{-1} < 0$, and $X'_1 > 0$. As can be seen, the stability limits under subsonic flow conditions are the same as the ones for the original impedance parameters R_0, X_{-1}, and X_{+1} given by Tam and Auriault [4]. Equation (12) is transformed back to the time domain using the auxiliary variable U'_n defined by $\dot{U}'_n = u'_n$. This yields the required condition to $\dot{u}'_n$ from the three-parameter model of Tam and Auriault using the effective impedance Z' given by Eq. (12):

$$\frac{\partial u'_n}{\partial t} = \frac{1}{X'_{+1}}[p' - R'_0u'_n + X'_{-1}U'_n] \tag{13}$$

In fact, the application of the effective impedance was mentioned earlier by Tam and Auriault, when they recognized an instability of the direct time-domain representation of the three-parameter model under flow conditions. This instability was first reported by Tester [3]. However, without a method to calculate the effective impedance, its application is not feasible. A method to approximate the effective impedance for one single frequency is described in the following subsection based on the idea of Li et al. [9].

Equation (10) is divided by $p(i\omega)$ and the impedance $Z(i\omega)$ is factored out to obtain an expression for the effective impedance $Z'(i\omega) = p(i\omega)/u_n(i\omega)$. The result is an expression for effective impedance of a linear liner under flow conditions [9]:

$$Z'(i\omega) = \frac{Z(i\omega)}{\kappa} \tag{14}$$

with the flow correction coefficient κ obtained from Eq. (10) as

$$\kappa = 1 + \frac{Z(i\omega)}{p(i\omega)}\boldsymbol{u}_0\cdot\nabla\left(\frac{p(i\omega)}{i\omega Z(i\omega)}\right) - \frac{1}{p(i\omega)}\frac{p(i\omega)}{i\omega}\boldsymbol{n}\cdot(\boldsymbol{n}\cdot\nabla\boldsymbol{u}_0) \tag{15}$$

The effective impedance from Eq. (14) is formulated in the frequency domain. The convective term and the curvature term lead to complex fractions in the definition of the effective impedance,

which disallows a general transfer of Eq. (15) to the time domain. To understand the approximation of κ found in Li et al. [9], Eq. (15) is rewritten under the assumption of a constant impedance:

$$\kappa - 1 = \frac{1}{p(i\omega)} \frac{1}{i\omega} \{ \boldsymbol{u}_0 \cdot \nabla p(i\omega) - p(i\omega) \boldsymbol{n} \cdot (\boldsymbol{n} \cdot \nabla \boldsymbol{u}_0) \} \tag{16}$$

There is a complex numerator $\{\ldots\}/(i\omega)$ and denominator $p(i\omega)$, which form a complex ratio for $\kappa - 1$. The complex ratio can easily be calculated in the frequency domain from the complex spectra of numerator and denominator. $\kappa - 1$ will be complex in general, which would make the method infeasible. However, to obtain an approximate and real time-domain representation of Eq. (16), it is required to restrict the model to a single-frequency sound source. This assumption seems to contradict the claim of a broadband time-domain boundary condition; the broadband boundary condition is chosen for the advantages in implementation anyway. For a single frequency, the ratio in the frequency spectrum falls back to the complex ratio of the two amplitudes of the harmonic waves. For a harmonic acoustic wave, the gradient and time integral of the pressure are connected. The expression $\{\ldots\}/(i\omega)$ includes the gradient of p and p itself. The derivative of the gradient will fall back to $-ip$ times a wave number vector, which is complex in general as the waves are attenuated along the liner. The curvature term remains real. The whole expression is divided by $i\omega$, which translates to a time integration. As long as the curvature term remains small compared to the convective term and the wave number in flow direction is approximately real, the expression Eq. (16) would also be approximately real. Under this assumption the complex expressions in Eq. (16) can be replaced by the amplitude of numerator and denominator. This can simply be calculated in the time domain. A better approximation may even be obtained using the root mean square of the parts in the time domain, which is the method chosen here. Considering a parallel orientation $(-)$ for a downstream propagating wave and antiparallel orientation $(+)$ for an upstream propagating wave, one obtains

$$\kappa \approx 1 \pm \frac{\langle s_p(t) \rangle_{\text{rms}}}{\langle p'(t) \rangle_{\text{rms}}} \tag{17}$$

As stated earlier, the expression for the numerator is obtained from $\{\ldots\}/(i\omega)$ of Eq. (16)

$$\frac{\partial s_p}{\partial t} = \boldsymbol{u}_0 \cdot p'(t) - \boldsymbol{n} \cdot (\boldsymbol{n} \cdot \boldsymbol{u}_0) p'(t) \tag{18}$$

The effective impedance depends on the Cosinus of the angle between the mean flow direction and the acoustic wave number vector. The preceding model is linear. As long as $||\kappa||$ is greater than zero, the limits given for the parameters of the aforementioned effective impedance transfer to the same condition for the impedance parameters. As the expression was derived from Myers boundary condition, this is the case for a subsonic flow.

Equation (17) was implemented to obtain the correction coefficient κ. Equation (18) is integrated by the LDDRK [18] to obtain s_p. Note: In the first publication of the EFI [9], the order to calculate the gradient and time derivative was reversed in the definition of s_p. In this paper the time integration is applied after the gradient of p' was calculated using the ghost-point pressure. This eliminates the need for an application of different finite-difference stencils at the wall for P' and p'. The integration of u'_n is also performed by the LDDRK [18]. The amplitude of s_p and p' are each calculated by the definition of the rms value. To obtain faster convergence, a sliding window, which is adjusted to a multiple of the frequency excited by the sound source, is used. Equation (17) is used to calculate the correction coefficient κ to obtain the effective impedance. Initially both amplitudes in Eq. (17) are zero; therefore, a starting period has to be defined with $\kappa = 1$. The effective impedance parameters are calculated from Eq. (14) and the boundary condition to $\dot{u}'_n$ in Eq. (8) is obtained from Eq. (13). The effective impedance parameters of the three-parameter model presented in the preceding subsection are evaluated as

$$R'_0 = \frac{R_0}{\kappa}; \qquad X'_{-1} = \frac{X_{-1}}{\kappa}; \qquad X'_{+1} = \frac{X_{+1}}{\kappa} \tag{19}$$

To evaluate the valid range for this approximation for a simplified example, a single mode in a straight axisymmetric duct is considered. The pressure perturbation is given by

$$p' = \hat{p}(r, \varphi) e^{i(\omega t - k_x x)}$$

using the axial wave number k_x and a pressure amplitude $\hat{p}$ containing all dependencies on r, φ. With a 1-D plug flow at $\boldsymbol{u}_0 = u_0$, Eq. (16) reads

$$\kappa - 1 = -\frac{\int_0^t u_0 (\partial p'/\partial x)\, \mathrm{d}t}{p'} = \frac{u_0 k_x}{\omega} \approx \frac{||u_0 k_x||}{\omega}$$

As long as the imaginary part of k_x remains small, the approximation of $u_0 k_x$ by $||u_0 k_x||$ from Eq. (17) is true and the EFI is well defined.

D. Extended Helmholtz Resonator Model

A time-discretized signal can be Fourier transformed by interpreting the sampled signal as a continuous signal multiplied by a series of delta functions in time. The inverse transform of the resulting periodic frequency-domain signal is a series of delta functions again. In the context of electromagnetism, these properties of the Fourier transformation are generalized to a theory referred to as z transformation. The application of this z transformation to a periodic impedance function $Z(i\omega)$ to obtain a more simple time-domain representation was first published by Özyörük and Long [5].

The following application of the z transformation to obtain the time-domain representation of the extended Helmholtz resonator model is following Rienstra [10]. The extended Helmholtz resonator model of Rienstra is defined in the frequency domain by

$$Z(i\omega) = R + i\omega m - i\beta \cot\left(\frac{1}{2} \omega T_l - i \frac{1}{2} \varepsilon \right) \tag{20}$$

$$= \frac{(R + i\omega m)(1 - e^{-\alpha}) + \beta(1 + e^{-\alpha})}{1 - e^{-\alpha}} \tag{21}$$

with $\alpha = i\omega T_l + \varepsilon$. All of the five parameters of this model R, m, ε, β, and T_l have to be positive to achieve a real, passive, and causal impedance $Z(i\omega)$ [10]. $Z(i\omega)$ is a rational function that describes a periodic frequency response of the impedance given by the function $e^{-i\omega T_l}$.

The derivation of a time-domain representation of the preceding model requires the application of a generalized δ function to obtain the inverse Fourier transform of a periodic functions $e^{-i\omega T_l}$:

$$\delta(t - T_l) = \frac{1}{2\pi} \int_{-\infty}^{\infty} e^{-i\omega T_l} e^{i\omega t}\, \mathrm{d}\omega \tag{22}$$

For a single-cavity type, undamped liner T_l would be related to the first antiresonance of the undamped cavity. With a cavity depth L and a speed of sound c, the periodicity in ω is then given by $\omega_0 = \pi L/c$. In general, Eq. (9) would lead to a convolution integral in the time domain. With a periodic frequency response of $Z(i\omega)$ which expands to a δ function, one obtains a single product

$$\frac{1}{2\pi} \int_{-\infty}^{\infty} z(\tau) \tilde{u}'_n(t - \tau)\, \mathrm{d}\tau = z_n \tilde{u}'_n(t - T_l) \tag{23}$$

By the definition of α, the aforementioned $Z(i\omega)$ is found to be a rational function of $e^{-i\omega T_l}$. The whole Eq. (21) of the impedance definition is to be multiplied by the denominator $(1 + e^{-\alpha})$:

$$(1 - e^{-\alpha}) \tilde{p}(i\omega) = [(R + \beta + i\omega m) - (R - \beta + i\omega m) e^{-\alpha}] \tilde{u}(i\omega)$$

Now the coherence Eq. (22) is applied to both sides using the properties of the inverse Fourier transformation given by Eq. (23):

$$\tilde{p}'(t) - e^{-\varepsilon}\tilde{p}'(t-T_l) = (R+\beta+i\omega m)\tilde{u}'_n(t) - (R-\beta + i\omega m)e^{-\varepsilon}\tilde{u}'_n(t-T_l) \quad (24)$$

Equation (10) is divided by $i\omega$, which means a time integration in the time domain. The $i\omega m$ term is transformed directly to a time derivative. The implemented form of the boundary condition to the time derivative of the normal velocity is given as

$$\frac{\partial u'_n}{\partial t}(t) = \frac{1}{m}[\mu(t) - e^{-\varepsilon}\mu(t-T_l) - (R+\beta)u'_n(t) + (R-\beta)e^{-\varepsilon}u'_n(t-T_l)] + e^{-\varepsilon}\frac{\partial u'_n}{\partial t}(t-T_l) \quad (25)$$

where $\mu(t)$ is defined with $\dot{P}' = p'$ as an abbreviation of the entire pressure dependent part from the Myers boundary condition:

$$\mu(t) = p' + \boldsymbol{u}_0 \cdot \nabla P' - \boldsymbol{n} \cdot (\boldsymbol{n} \cdot \nabla \boldsymbol{u}_0)P' \quad (26)$$

As discussed in the preceding section, it is inconvenient to calculate derivatives of the time integral. Therefore the time integration is performed after the spatial derivative. This yields a large similarity between the two models. If we use the definition of κ from Eq. (15), $\mu(t)$ can also be expressed as

$$\mu(t) = p'\kappa = p' + s_p \quad (27)$$

Equation (27) combined with Eq. (25) represents the implementation form of the EHR.

We deliberately choose the full extended Helmholtz resonator with nonzero face-sheet mass reactance. If m of an impedance surface defined by Eq. (20) is sufficiently large, the coupling of the EHR to the flow through this parameter becomes possible. In addition, for cases with nonzero m, the numerical implementation of the EHR is more similar to that of the EFI and the numerical stability for the EHR is found to be advanced for this form. We assume to have at least a small face-sheet [12] reactance, which is similar to the assumption of Chevaugeon et al. [11] under mean-flow conditions.

The EHR requires the data at previous times $t - T_l$. As the coefficients are constant, the whole expression including old time levels can be stored in one variable. To avoid interpolation, T_l could be chosen to be a multiple of the time step of the time-domain simulation. This was originally mentioned in the paper of Rienstra [10]. This would especially be a good choice for multi-time-step high-order schemes. However, for algorithms using a Runge–Kutta scheme for time integration, the interpolation could not be avoided. Therefore, we do not need to fix the period time T_l to a multiple of the time-step size. The implementation of the EHR requires the same integration as the EFI to evaluate s_p from Eq. (18). The LDDRK is used for the time integration. All terms explicitly showing T_l in Eq. (25) are summed and stored for every full time step of the LDDRK. This is implemented using a circular buffer. Old time levels up to ten time steps before $t - T_l$ are stored. A cubic, spline interpolation is used to obtain the value at $t - T_l$. The actual time derivative $\dot{u}'_n$ is obtained from Eq. (25). The frequency response of the impedance is based on the definition Eq. (20).

IV. Results and Discussion

Two benchmark problems are considered for both the EFI and EHR. The results are organized into the following subsections: In Sec. IV.A the NASA Grazing Incidence Tube experiment is used as the validation. In Sec. VI.B the second benchmark problem involves the sound propagation in a fully lined generic engine with hard walled spinner. The results from both models are compared with that of Rienstra and Eversman [13]. The broadband application of the EFI and EHR is discussed in Sec. IV.C. The application of EHR as open-end termination impedance is shown. Finally, an impedance eduction is carried out to obtain a globally-fitting liner impedance for EHR by coupling the CAA method with the optimization tools of MATLAB.

A. Validation with the NASA Grazing Incidence Tube Experiment

The latest measurement of a ceramic tubular liner at the NASA Grazing Incidence Tube (GIT) [14] is used to validate both time-domain impedance models. Because EFI and EHR were designed to include mean-flow effects, a case with higher flow Mach number $M = 0.4$ but still fully reliable experimental results is chosen.

1. Numerical Setup

The flow-impedance testing experiment is approximated by a 2-D model in the computation. The dimensions used in the computation are directly from the experimental configuration. The numerical grid and the boundary conditions are summarized in Fig. 2. We first focus on the results obtained with nonreflective terminations within this section. The results using the termination impedance together with the liner impedance are given in Sec. IV.C. The setup shown in Fig. 2 is extended by a PML [Eq. (5)] downstream the terminal plane to obtain a reflection free termination. Unlike the numerical model applied by Watson et al. [15] the sound source is always assumed nonreflective to upstream propagating waves. The reflection free boundary condition upstream is achieved by the sponge layer of Eq. (6).

To allow the impedance jump from the hard-walled inlet duct to the lined section and from the lined section to the hard-walled outlet duct, the computation domain is decomposed into three blocks. These blocks exchange all field data and each grid point is calculated in only one block. There are very short waves present in the acoustic field in reaction to the impedance jump at these interfaces. The explicit time-integration method and the finite-difference scheme are very susceptible to these short waves. Therefore, it is required to filter all variables that are derived subsequently. The filtering step is performed every other time step. As a side effect of the numerically motivated filtering, the streamlines pass smoothly across the edges between the hard wall and the liner. The variables connected to old time levels $(t - T_l)$ in Eq. (25) have also to be filtered to guarantee stability for the EHR. Similar observations were reported by previous studies using the Myers boundary condition [6,10,11,25]. The current authors [12] and Chevaugeon et al. [11] simultaneously published the possibility to shield a possible instability out by filtering or smoothing of the old time levels. The filtering is not required for the EFI using the fine mesh. However, this is not necessary when using EFI.

The mean-flow profiles used in the computation are interpolated from the Pitot probe measurements given by Jones et al. [14] for the axial position above the liner. Because the experimental data supports the assumption of a fully developed laminar profile, the wall velocity of $u_0 \approx 85$ m/s was extrapolated by a parabolic law. The viscous layers are not resolved in the simulation but covered by the Myers boundary condition. The educed impedance values given by Jones et al. [14] for the 406 mm long liner are used. The computed

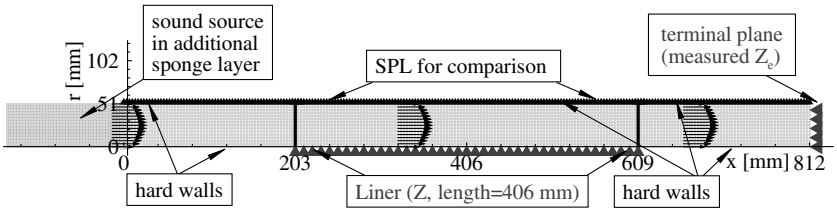

Fig. 2 Numerical model for the NASA GIT [14] (height coordinate flipped with respect to the reference).

sound pressure level (SPL) at the opposite hard wall is then compared to the corresponding measured values. The typical turnaround time is 20 min for 30,000 time steps. The Courant–Friedrichs–Lewy (CFL) number must be chosen to be 0.15, as the EHR shows a numerical instability for some cases with a higher CFL number. The EFI is more robust with respect to large time steps. The uniform grid size is $\Delta x \approx 3.4 \times 10^{-3}$ mm and the time-step size $\Delta t = 1.0 \times 10^{-6}$ s.

2. *NASA GIT Validation and Verification of EFI and EHR*

In general, notably similar results are obtained for both models (see Fig. 3). The predictions of both models only differ significantly for the case of 3 kHz. Consequently, the numerical results of both models agree well with the experiment for most of the cases. Especially the cases in the frequency range around the antiresonance (2 kHz) of the ceramic tubular liner are well met. Interestingly, both models fail completely for the case of 1 kHz.

Small differences at the leading and trailing edges of the liner are due to the filtering of the old time levels of the liner variables for the EHR. A equivalent filtering of $\langle s_p \rangle_{\mathrm{rms}}$ is not necessary and not performed for the EFI. Therefore, the predictions for the sound pressure level differ in these regions. A very interesting observation from Fig. 3 is the different attenuation slopes in the case of 3 kHz. The EFI is not able to predict the strong attenuation in this case. One of the main assumptions of the EFI is violated as the wave number in flow direction is probably not even approximately real for the second resonance of the liner. Consequently the models provide different predictions in this case. For the EHR, however, no such limitation applies. As a result, the prediction is closer to the experiment.

Among others, one possible explanation for the observed discrepancy between experiment and numerical simulation is the presence of an instability in the region around 1 kHz. This spatially growing instability wave was discussed in detail in Li et al. [9]. When the instability wave impinges to the wall downstream to the liner, it excites acoustic waves. This leads to an increase of the SPL at the upper wall around the trailing edge of the liner. The instability wave was shown to be connected to the type of mean-flow profile used [9]. However, the linear model using the interpolated mean-flow profile from a pitot probe measurement must fail to predict the amplitude of the instability correctly. Therefore, it could not be decided with final confidence that an instability causes the steep decay to stop as observed for both the experiment and the simulation around $x =$ 450 mm right 150 mm before the end of the liner. Another possible explanation covering the observed differences for both 3 and 1 kHz is a nonlinear amplitude dependency of the resistance or the whole impedance. The normal velocity perturbation at the surface reaches a maximum around the resonances of the ceramic tubular liner. A possible nonlinearity could most likely be observed for the highest normal velocities at the lined surface.

Finally, in the case of 500 Hz, the CAA results do not follow the experimental data. The measured impedance in this case is somehow out of the range. The authors who conducted the measurement assume a reflection or standing wave in the entire test section in this case. This reflection could not be predicted without a given termination impedance for both ends of the test section.

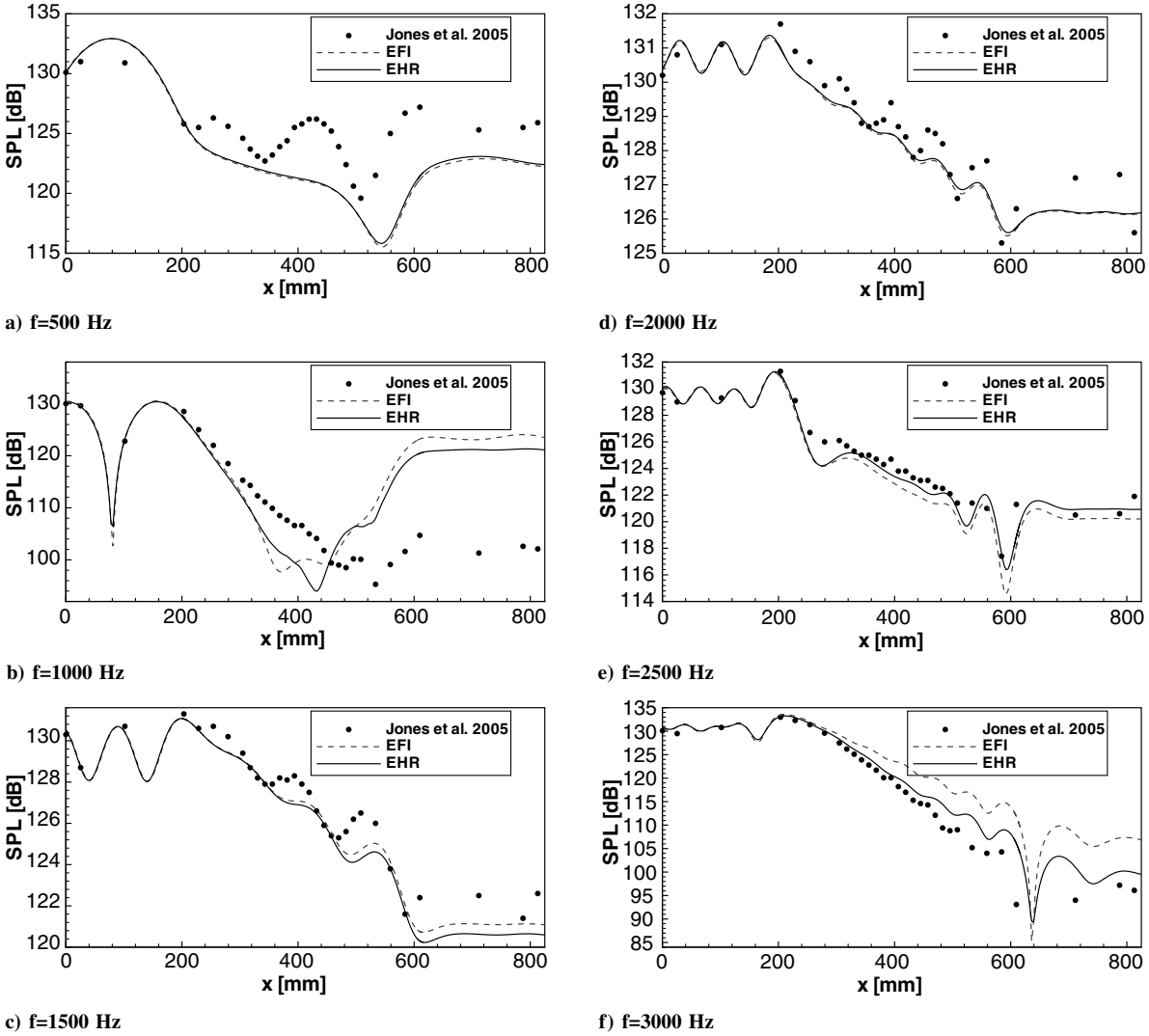

Fig. 3 Comparison between EHR, EFI, and experiment [14] for the NASA GIT with nonreflecting outlet.

B. Generic Aeroengine Benchmark Comparison

In this section, EFI and EHR are to be compared by using a more realistic geometry. To evaluate the possible application of both models in the design of aeroengine inlets and numerical support of test rig experiments, an axisymmetric aeroengine inlet is chosen. However, there is a lack of published sources for axisymmetric realistic curved inlet geometries containing a reasonably broad spectrum of experimental and numerical results for comparison. Therefore a generic aeroengine inlet geometry investigated only numerically [13] is chosen for the verification of the two models. The database provided by Rienstra and Eversman [13] comprises the results for hard and impedance walls with higher modes at realistic frequencies, propagating through an axisymmetric aeroengine inlet with spinner. Only the in-duct propagation is considered, as the semi-analytical method used in the reference [13] is not intended to cover radiation problems. The outer wall of the inlet is fully lined to provide the necessary condition of slow variation for the semi-analytical multiple scales method (MS) used in [13]. Therefore, there is no impedance jump. The impedance is constant $Z = 2 - i$ for all considered frequencies.

The aforementioned limitations are unnecessary restrictions to the current method, and the impedance is relatively large when compared to the measured impedances around the most sensitive resonance. However, the generic aeroengine inlet provides a large purely numerical database as a benchmark source for the EFI and EHR. In this comparison the result obtained by a finite element frequency-domain method (FEM) are considered as the reference solution. The multiple scales method also used within the referenced paper does not include reflected waves due to the area change and mean flow as well as mode scattering. These may be important effects for the considered generic aeroengine inlet geometry as it was shown by Li et al. [26].

Among the cases considered by Rienstra and Eversman [13], we have chosen the ones with a single, cut-on, higher azimuthal mode propagating against the mean flow at $M = 0.5$. Different from the straight duct considered in the preceding section, in this section convective and curvature terms of the Myers boundary condition contribute to the solution. Even though the curvature term may be small due to the slow variation in geometry, the cases provide a full verification of the implementation. The mean flow shown in Fig. 4 is used in the CAA calculations. It is interpolated from the one used for the MS solution by a nearest-neighbor method and smoothed in a filtering process. The eigenvalues for the modes are also the same as that used by Rienstra and Eversman. The sound source is a single mode, which is implemented according to Sec. II in the region $x < 0$. Within a multiblock of 45×151 grid points, a damping distribution is defined for the sponge layer of Eq. (6). The inlet plane is considered nonreflective by the PML boundary condition of Eq. (5).

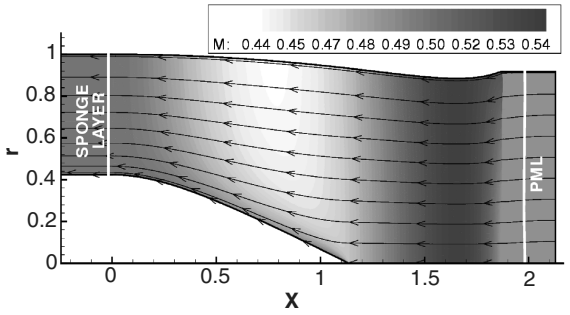

Fig. 4 Sketch of the generic inlet; the mean flow is taken from Rienstra and Eversman [13].

The generic aeroengine inlet problem is formulated nondimensional, with the outer radius at the fan plane, the speed of sound at the fan plane, and the density at the fan plane. The mesh for the CAA computation consists of 12 blocks of altogether 78,012 grid points. The grid is body fitted. Because of the unnecessary high block segmentation, 25,300, or 32% of the grid points, are used to incorporate the boundary conditions and block interfaces. The typical axial resolution of the grid is about $\Delta x = 0.0054$. The time step is chosen to be $\Delta t = 7 \times 10^{-2}$. For each of the cases, 25,000 time steps are calculated. This takes about 5 h on a Pentium IV desktop with 3 GHz.

The refined mesh used in Fig. 5 consists of only two blocks with altogether 145,389 points. The typical mesh size is $\Delta x = 0.0029$, which could be reached by a reduced overhead of only 10.5% or 15,276 points to implement boundary conditions and block exchange. The typical time-step size was reduced to $\Delta t = 2.5 \times 10^{-2}$ for the refined mesh.

Figure 6 shows the results of Helmholtz number $\omega = 16$ for a $\nu = 10$ first radial mode. The mesh resolves this mode axially with 49.2 points per wavelength (PPW). The results using both the EFI and EHR compare well with each other. The attenuated sound field within the lined inlet predicted by the current CAA method compares well with the one obtained by the FEM method [13]. However, the amplitude at the inlet plane right in the figures is about 20% smaller when compared to the one predicted by FEM.

The results for $\nu = 10$, $\omega = 50$ are shown in Fig. 5. The axial resolution is reduced to only 11.8 PPW in this case. The solutions of the EFI and EHR compare well with each other.

However, there are some outstanding differences when comparing the CAA solutions to the FEM as well as MS solutions [13]. The lip region of the inlet with $x > 1.7$ shows a different location of the main lobe, especially. It does not point inside for the benchmark source as it was observed with the CAA method. Additionally, the pressure amplitude within this region is higher than in the reference solutions. This leads to a different relative pressure field, as it is normalized by the maximum value found in the lip region for this case.

The aforementioned case is the one with the lowest axial resolution. Therefore, a grid refinement study was carried out for this case. The solution obtained using the refined grid with an axial resolution of 22.3 PPW is very similar to the one using the coarse grid as shown in Fig. 7b. The most outstanding differences are observed in the small amplitude regions in front of the spinner. There is in particular no significant change of the general shape of the main lobe obtained by the axially and radially refined and redesigned mesh.

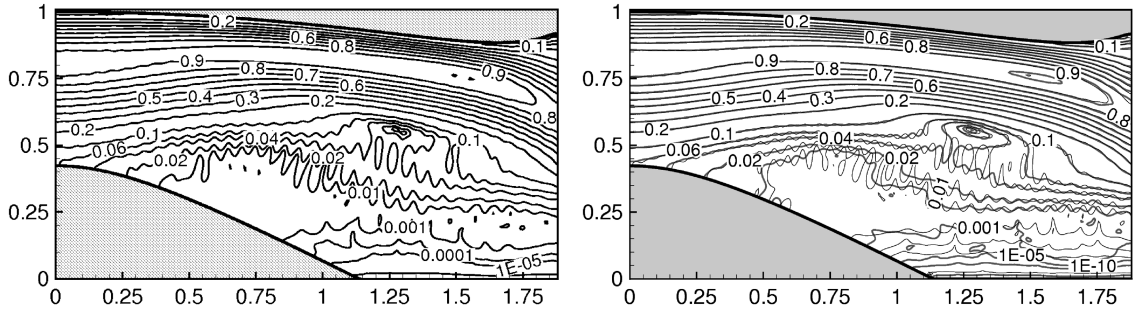

a) EFI b) EHR

Fig. 5 Comparison of relative pressure contours ($\nu = 10$, $n = 1$, $\omega = 50$).

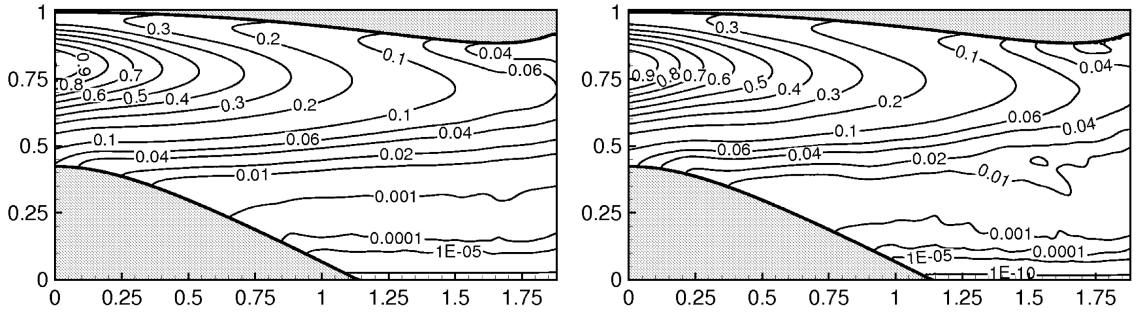

Fig. 6 Comparison of relative pressure contours ($\nu = 10$, $n = 1$, $\omega = 16$).

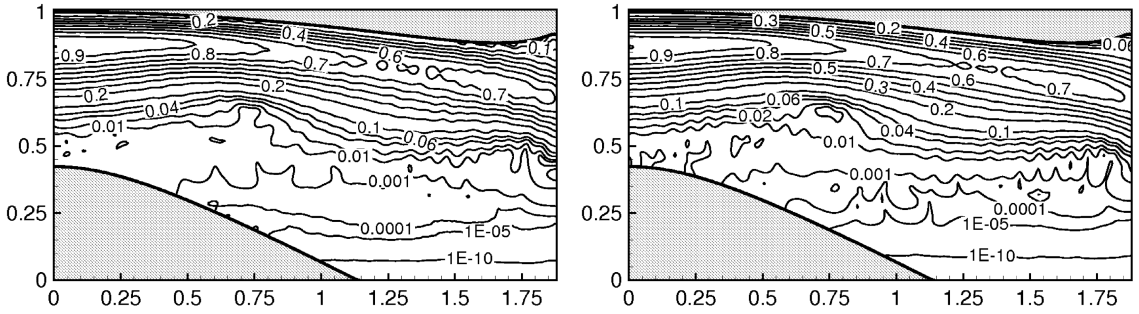

Fig. 7 Comparison of relative pressure contours ($\nu = 20$, $n = 1$, $\omega = 50$).

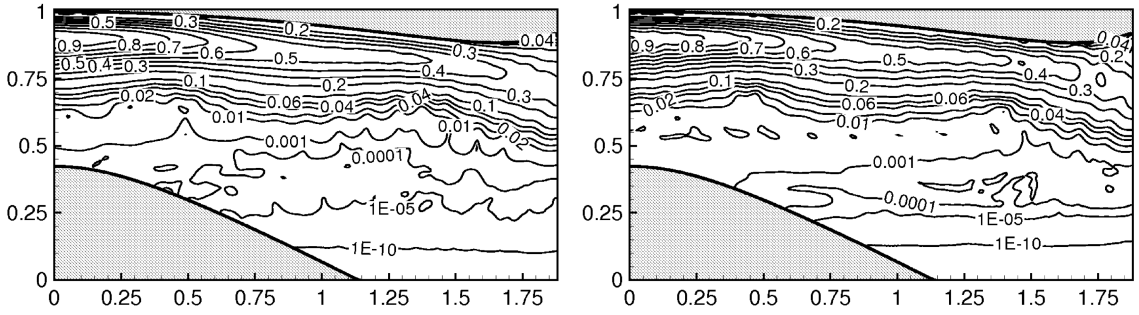

Fig. 8 Comparison of relative pressure contours ($\nu = 30$, $n = 1$, $\omega = 50$).

The results for the case of $\nu = 20$, $\omega = 50$ are summarized in Fig. 7. The axial resolution is 12.4 PPW. Even though the EFI uses an approximation of the effective impedance, it produces an overall very similar result as the EHR. The relative pressure contours of the EFI and EHR are very similar to the ones obtained by the FEM solution [13]. However, the FEM [13] solution shows a 12% higher pressure amplitude within the main lobe around the lip region.

The results summarized in Fig. 8 show the CAA results for an azimuthal mode of $\nu = 30$, $\omega = 50$. The axial resolution is 13.6 PPW. The agreement between the EFI and EHR is good. Only small differences are observed in the region in front of the spinner showing small amplitudes anyway. Similar to the other cases, the attenuation is predicted slightly higher for both the EFI and EHR when compared to FEM [13]. For example, the contour of $\hat{p}/p_{\max} = 0.4$ ends at $x = 1.7$ for the CAA simulations instead of $x = 1.8$ obtained by FEM [13]. The region upstream of the lip shows even larger differences when compared to the reference. However, the general qualitative agreement of the normalized pressure contours between CAA and FEM [13] is also good for this case.

The highest azimuthal mode number used in the reference of Rienstra and Eversman is $\nu = 40$ [13]. This mode is axially resolved by 16.6 PPW when propagating at $\omega = 50$ against the flow. The CAA results are summarized in Fig. 9. Both of the CAA solutions agree well with each other. The attenuation is slightly larger than [13] for both the EFI and EHR solutions. The qualitative agreement of both models to the FEM [13] solution is good again. Even the acoustic field in the low-amplitude regions around $x = 0.2$, 0.4, and 0.6 is predicted correctly.

In general, the presented time-domain impedance models, EFI and EHR, are in a notably good agreement with each other. The solutions from both models are close to the FEM [13] solution, although they always show smaller amplitudes in the lip region of the generic inlet. The refined mesh shows no significantly different dissipation characteristics for the $\nu = 10$ mode. This is the mode minimally resolved by the coarse mesh before. The case with the highest resolution considered here does also show this lower amplitudes with the current CAA method. Numerical dissipation would always depend on the grid size; therefore, the obvious assumption of numerical dissipation due to the CAA method can be dropped. Apart from small roundoff and interpolation errors, the mean flow and modal shapes are exactly the same as used for the MS solution. This possible reason for a large difference [16,26] can therefore also be dropped.

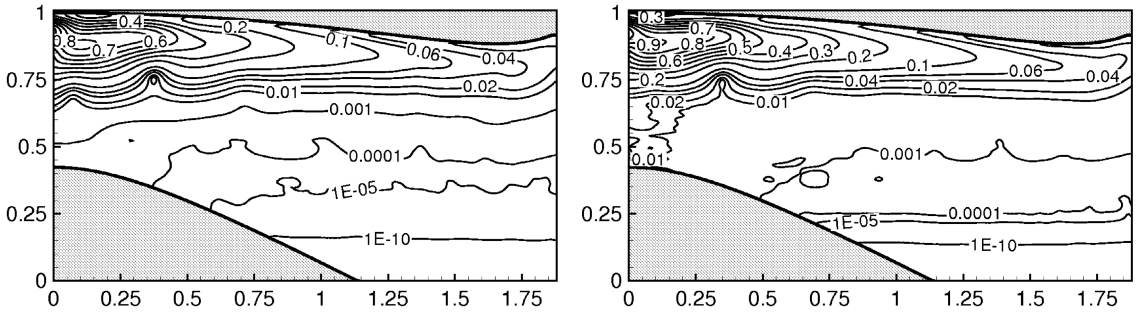

a) EFI b) EHR

Fig. 9 Comparison of relative pressure contours ($v = 40$, $n = 1$, $\omega = 50$).

There is no explanation for the different directivity of the main lobe observed for one of the cases. A strong, rotational component within the interpolated and filtered mean flow due to the assumed wall compatible radial velocity could be excluded by the comparison to a potential equivalent mathematical model in the CAA simulation [12]. Entropy or vorticity perturbations are not anticipated to propagate in the inlet and were also excluded by the potential equivalent model [12].

The remaining possible reasons for the observed difference between CAA and FEM [13] are different boundary conditions upstream the lip of the inlet and at the sound source. The CAA computation uses additional grid lines to implement nonreflective boundary conditions here. The outer wall of the regions is assumed to be lined to avoid an impedance jump. The treatment of these regions by the FEM is not discussed in detail in [13]. Therefore no final analysis of the differences is possible, but a partial reflection due to the FEM boundary conditions would be one possible explanation.

C. Broadband Impedance Fitting by EHR and EFI

The preceding subsections limited the numerical calculations to single-frequency cases. However, for realistic applications of time-domain impedance models, it is crucial to fit the frequency response given by the models to real impedance data. Only if the fitting is possible for a sufficiently large range of frequencies, the time-domain impedance model can effectively be used to solve the broadband and nonlinear problems.

1. *Theoretical Comparison of EFI and EHR*

Both models have some flexibility to allow the fit of the frequency response of the impedance. However, the EFI is very limited in this point. Because the approximation of the model to obtain the effective impedance under flow conditions requires a single frequency source, the EFI is no broadband model at all in its current form. Even if this limitation could be dropped, strong limitations inherited from the three-parameter model remain. The valid range of the reactance parameters allows only positive slopes for the effective reactance. Furthermore, the zeroth-order resistance parameter limits the EFI to a constant resistance for all frequencies. Overall, the EFI in its current form is not suitable for broadband time-domain computations. The EHR, on the other side, does not have any of these limitations. As the model is physically motivated, it may fit very well to real, single-cavity Helmholtz resonator type liners.

Both the EFI and EHR employ the Myers boundary condition as the basic definition of the impedance under mean-flow conditions. The Myers boundary condition is implemented for both models by coupling the solution at any given time to the respective solutions at previous time levels. The EFI requires only three variables per wall point as it uses averaged values. The EHR requires the time history of one variable back to time level $t - T_l$ to be stored.

For a single-frequency, small-attenuation, small-curvature case, both models are of equal usability. The EFI is preferable for tonal 3-D applications, because it uses less memory than the EHR. The initially stated transient or broadband problems require the application of the EHR. The computational time for both models is approximately equal. The EFI requires a time integral of the velocity, which is not necessary for the EHR, but the EHR requires an interpolation of solutions at various previous time levels and a filtering of the variables, which is approximately equivalent to the time integration.

2. *Fitting of Impedances by EHR*

Within this section the database of Jones et al. [14] is used to assess the potential of EHR in fitting realistic liner impedances. To demonstrate the capability of EHR, the periodic behavior of a measured terminal impedance is fitted first. The impedance values obtained by Jones et al. [14] are used. A constrained nonlinear MATLAB optimization fits the five parameters for the EHR of Eq. (20) to the given frequency response of the termination impedance. To keep the impedance physical, all five parameters are restricted to be positive during the optimization. In addition, a constraint on the parameter m is added: $1/m \leq 2000$, to allow the coupling of the EHR through m in Eq. (25). If the face-sheet reactance described by m is too small in Eq. (25), the coupling between lined surface and sound propagation in the fluid would be weak. As can be seen from Fig. 10, the fitted resistance and reactance agree well with the measured impedance at the open terminal plane. The five parameters of the EHR fitting the termination impedance best are obtained as

$$R_{\text{end}} = 0.7316; \qquad \beta_{\text{end}} = 0.2685; \qquad \varepsilon_{\text{end}} = 1$$

$$\frac{1}{m_{\text{end}}} = 2000; \qquad \frac{1}{T_{\text{end}}} = 346.8$$

The boundary condition used at the termination plane is given according to Watson et al. [15] as $\mu(t) = p'(t)$. The aforementioned impedance definition is used for the EHR instead of Eq. (26) in the following. Different from the boundary condition of the liner, there is no Myers boundary condition used for the termination impedance [15].

The same procedure is now used to find a set of five parameters fitting the frequency response of the liner impedances educed by Jones et al. [14]. The frequency response of resistance and reactance of the optimum set is presented in Fig. 10. The EHR obviously does not fit the liner impedance very well for the higher frequencies. With a weighting function, the discrepancies could be shifted to the lower frequencies. However, a good fitting by the EHR is cumbersome. The period of the measured impedance is around 2 kHz. There is a sufficient number of data points to be fitted by the EHR. The impedances in the ranges between 2.5–3 kHz and 0.5–1.0 kHz should be almost equal for an antiresonance around 2 kHz. The face-sheet reactance parameter $m > 0$ adds a linear increase of the reactance with the frequency. However, to fit the measured data, $m < 0$ would be required. CAA computations using the fitted impedance reinforce the assumption that the EHR using this parameter set would not agree with the measured SPL data. Therefore, this concept of fitting the liner impedance is not followed within this paper. In the following section, the five parameters of the EHR are educed from the measured acoustic data for the ceramic

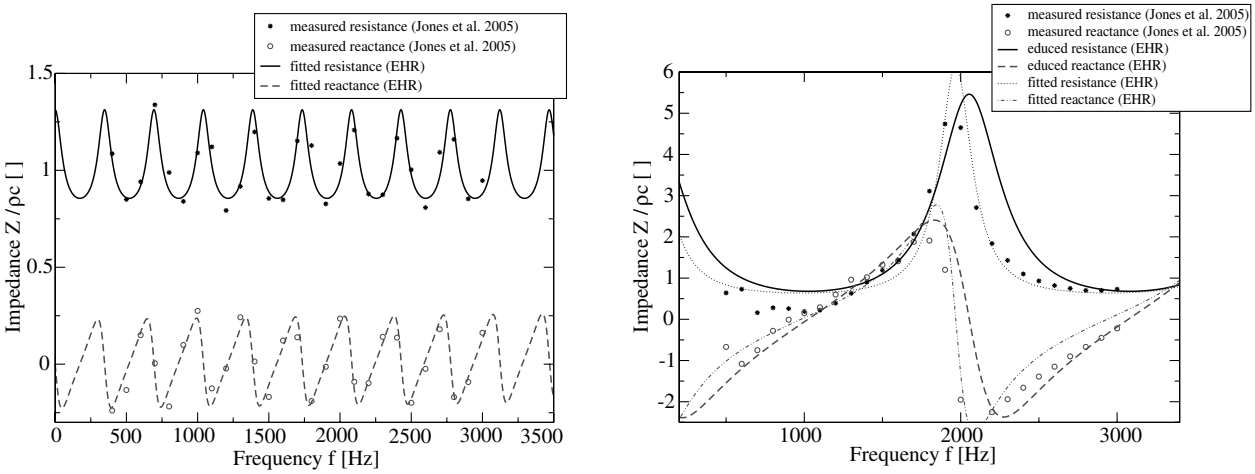

a) EHR fit to the measured end impedance **b) EHR fit and educed liner impedances**

Fig. 10 Frequency response of liner and termination impedance.

tubular liner. The broadband capability of the EHR will demonstrated with the educed impedances instead of the fitted ones.

3. *Eduction of the Liner Impedance by Optimization*

The eduction process employs the CAA method to find an impedance function that best fits the measured sound attenuation. Jones et al. used an impedance eduction for each single frequency and did not assume a connection between the different frequencies [14,15]. With the potential of EHR it is possible to educe one single parameter set for an extended Helmholtz resonator, which fits the measured SPL best for all frequencies. The eduction is carried out using a broadband source that excites all 26 frequencies considered in the experiment. From the large test matrix considered in the experiment, the case of plane waves propagating at 130 dB with a flow of $M_{\max} = 0.4$ is chosen.

The MATLAB optimization tool is coupled to the CAA method to calculate the objective function. The so-called medium-scale algorithm of the constrained nonlinear *MATLAB* optimization procedure *fmincon* is used. Gradients are calculated by additional calls of the CAA method through the MATLAB function. The two broad curves for the educed resistance and reactance, respectively, given in Fig. 10, are obtained under the constraint that all five parameters of EHR are positive [10]. Additionally, due to the periodicity of the impedance function, the valid range for $(1/T_l)$ has to be fixed in the optimization. $1/T_l$ is limited by an indirect constraint to the range 1985.95 ± 200 Hz around the undamped antiresonant frequency calculated based on the cavity depth of 85.6 mm. The initial values of the parameters for the optimization for the presented results were chosen to be

$$R_{\text{initial}} = 0.35; \qquad \beta_{\text{initial}} = 3.0; \qquad \varepsilon_{\text{initial}} = 0.1625$$
$$\frac{1}{m_{\text{initial}}} = 500; \qquad \frac{1}{T_{\text{initial}}} = 1985.98$$

The time history of 0.01 s within 9540 time steps for each of the microphone positions except for the one behind the exit plane is recorded and stored. The calculated amplitude and phase values are normalized to fit the average of the first three microphones. The objective function is defined by the sum of all 26×28 relative amplitude errors measured in dB and the modulus of the relative phase error with respect to π. The results of the simultaneous optimization for the five parameters based on the latest measured SPL data of Jones et al. [14] are shown in Fig. 10. The optimal fitting impedance parameters are found after 37 optimization steps taking 338 function calls within six days, which equals approximately 25 min per function call on a Pentium IV, 3.0 GHz:

$$R_{\text{edu.}} = 0.000926; \qquad \beta_{\text{edu.}} = 1.925; \qquad \varepsilon_{\text{edu.}} = 0.7367$$
$$\frac{1}{m_{\text{edu.}}} = 2136.5; \qquad \frac{1}{T_{\text{edu.}}} = 2054.5$$

The face-sheet resistance and the reactance are found to be very small for the faceless, ceramic tubular liner. The cavity-resistance parameter ε is quite large, which is in a good agreement with the assumption of Jones et al. [14]. The global error distributions for the optimal parameter set (relative error in dB and phase error) are shown in Fig. 11. A more detailed discussion of some specific cases is given in the following section.

4. *Applications of EHR Model as a Broadband Impedance Model*

The same frequencies as in Sec. IV.A. are picked for comparison again. The relatively good broadband fit of the termination impedance by the EHR (see Fig. 10) is consequently used instead of the nonreflective boundary condition. The globally educed liner impedance is compared to the result obtained using the exact liner impedances for each frequency given by Jones et al. [14].

Figure 12 shows the decay of the SPL along the wall opposite to the lined surface for the globally educed Z and the impedance given by Jones et al. [14] in comparison to the experimental data. Because of the application of the termination impedance in Fig. 12, the agreement to the experiment has been improved for nearly all cases in comparison to Fig. 3. The globally educed impedance shows a similar good result. For the lower-frequency cases the agreement with the experiment is even improved by the educed impedance. From Fig. 12 it can be noted that the SPL at the terminal plane is accurately predicted within the range of 1 dB by the globally educed impedance. The agreement for the 500 Hz case is improved with the globally educed impedance (see Figs. 3 and 12). Although the differences in SPL at some locations are around 3 dB for the globally educed impedance, they were 5 dB with the impedance given by Jones et al,

For the case of 1 kHz, the results of both impedance values show the effect of the possible flow instability. The amplitude is reduced from that observed in Fig. 3 using a nonreflecting termination boundary condition. The increased sound pressure level at the opposite wall is reduced by the interference of excited and reflected waves from the impedance termination. However, the SPL in the outlet duct is still overpredicted by the exact liner impedance. The globally educed impedance fits these microphones better, but the slope for the lined section is wrong. The eduction fails to get the correct attenuation slope along the liner in this case in favor of fitting the values in the outlet duct correctly. As seen from Fig. 11, the problem concerns the frequency range from 1.0 to 1.2 kHz.

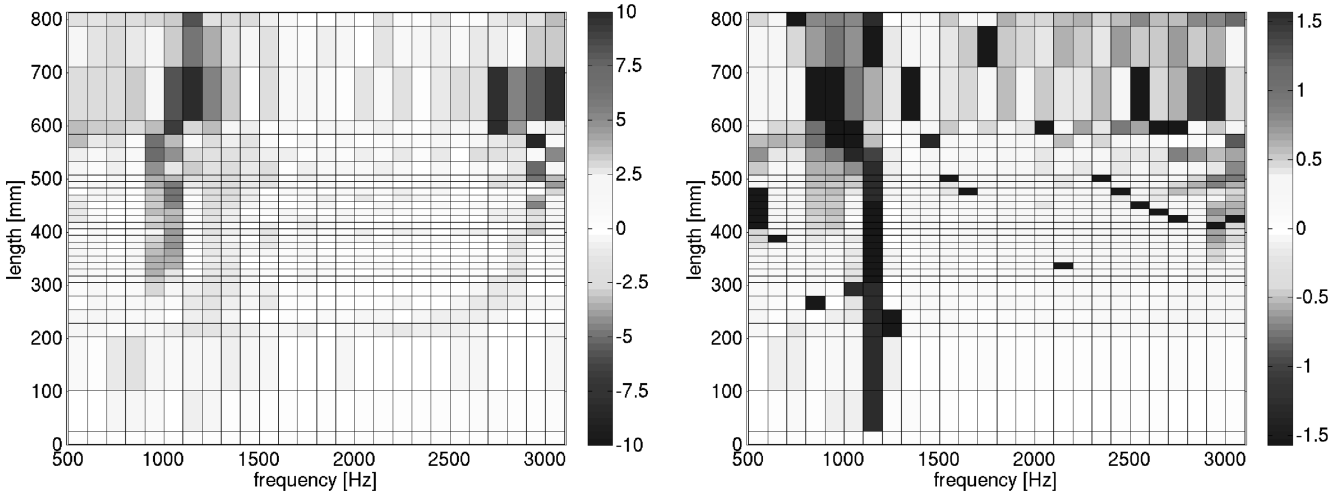

a) Relative amplitude error (dB)

b) Absolute phase error (rad)

Fig. 11 Error after the optimization process.

Comparing the frequency response of the impedance in Fig. 10, the educed impedances show a large difference in the near region of the antiresonance (around 2 kHz). The agreement between the impedance value given by Jones et al. [14] and the globally educed impedance value is very poor for this region, whereas the smaller impedances values are met by the current eduction. It is difficult to obtain the impedance in the region of an antiresonance, when only considering one frequency [15]. The EHR adds modeling

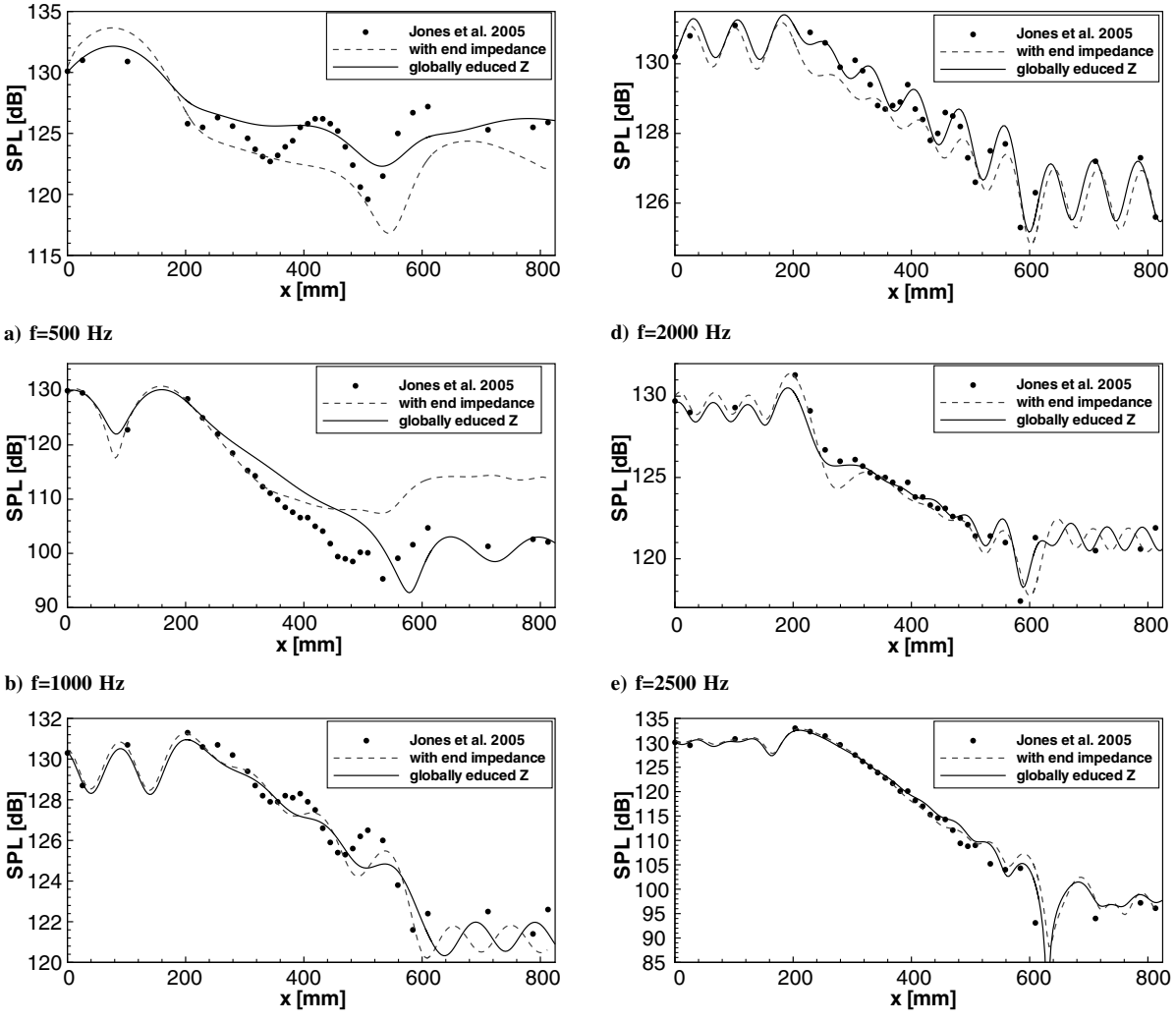

a) f=500 Hz

d) f=2000 Hz

b) f=1000 Hz

e) f=2500 Hz

c) f=1500 Hz

f) f=3000 Hz

Fig. 12 Comparison between the educed and given impedances (see Fig. 3) using the measured termination impedance at the NASA GIT.

information to the eduction process. Not the impedance for each frequency is actually educed, but the parameter set of an extended Helmholtz resonator. The antiresonance is influenced by the resonance points too. Figure 11 shows no increased errors due to the different impedance values in the region surrounding the antiresonance. The physical interpretation of the impedance parameters substantiates that the impedance function representing the ceramic, tubular liner through the EHR may be physically correct. However, to prove the uniqueness and sensitivity of the solution, a systematic variation of the initial parameter set is required. This is outside the scope of this paper. In summary, using the NASA GIT data it was shown that, at least for simple problems as open-end impedance and single-cavity liners, the EHR can be considered as an adequate model.

V. Conclusions

Two time-domain impedance models developed recently have been implemented to a time-explicit CAA method based on an optimized finite-difference discretization. The linear effects of the liner curvature and the mean flow on the impedance are correctly modeled by both models using the boundary condition of Myers [2]. A validation and verification is performed for the NASA GIT experiment and a lined generic aeroengine inlet with spinner. These benchmark configurations cover 2-D problems with plane waves and axisymmetric problems with higher azimuthal modes at high frequencies, respectively. Results from both models in general agree notably well with each other for the two benchmark problems.

For single-tone problems, the EFI provides the same prediction as the EHR in most of the cases. However, some cases show the limitation of the EFI for solving acoustic problems with a harmonic source and approximately real wave numbers in flow direction at the only light curved lined surface at the moment. For single-frequency cases, the agreement between the time-domain impedance models and the NASA experiment [14] is, in general, good. The measured termination impedance for the nonperfect, nonreflective open termination can reduce the observed differences. Among others, a possible flow instability of Tollmien–Schlichting type in the region of 1 kHz or nonlinear effects changing the impedance properties around the resonance of the liner may explain the observed problems to predict these cases correctly.

For the generic aeroengine inlet [13], the results obtained with the two models agree notably well with each other. The qualitative shape of the reference solutions in the frequency domain is meet for most of the cases. Essential differences are only observable for the lip region. The sound pressure amplitude in the lip region of the aeroengine inlet is between 10 and 20% smaller than it was predicted by the FEM solution [13] for all cases. A grid-refinement study was carried out with no essential different result. Independently of the resolution, higher amplitudes are always observed for FEM in the lip region. This was associated to a different treatment of the nonreflective boundary conditions by CAA and FEM. The results, however, demonstrate that both the EFI and the EHR provide correct and effective predictions for such simplified tone noise problems.

EFI in the presented form is not applicable for broadband problems. An instability could be observed when using the EHR. It is shielded out by filtering the old time levels in the current study. EFI does not require an separate filtering of the time levels. EHR has been demonstrated to be effectively used for broadband acoustic problems. The measured termination impedance of the NASA Grazing Incidence Tube could be directly fitted by the EHR. However, the frequency response of the liner impedance given by Jones et al. [14] for a ceramic, tubular liner could not be fitted. The successful eduction of a broadband impedance with the EHR from the acoustic measurements could demonstrate the capability and potential of the model nevertheless. The resulting educed impedance parameters show an excellent agreement with the experiment for all frequencies except in the region where the flow instability occurs.

Acknowledgments

The authors gratefully acknowledge the financial support through LiMiT, CombustionNoise, NSFC-10472010, and ASFC-05C51030, and by the German Academic Exchange Service, which made the international cooperation possible.

References

[1] Ingard, U., "Influence of Fluid Motion Past a Plane Boundary on Sound Reflection, Absorption, and Transmission," *Journal of the Acoustical Society of America*, Vol. 31, No. 7, July 1959, pp. 1035–1036.

[2] Myers, M. K., "On the Acoustic Boundary Condition in the Presence of Flow," *Journal of Sound and Vibration*, Vol. 71, No. 8, Aug. 1980, pp. 429–434.

[3] Tester, B. J., "The Propagation and Attenuation of Sound in Lined Ducts Containing Uniform or Plug Flow," *Journal of Sound and Vibration*, Vol. 28, No. 2, 1973, pp. 151–203.

[4] Tam, C. K. W., and Auriault, L., "Time-Domain Impedance Boundary Conditions for Computational Aeroacoustics," *AIAA Journal*, Vol. 34, No. 5, May 1996, pp. 917–923.

[5] Özyörük, Y., and Long, L. N., "A Time-Domain Implementation on Surface Acoustic Impedance Condition with and Without Flow," AIAA Paper 1996-1663, May 1996.

[6] Özyörük, Y., and Long, L. N., "Time-Domain Calculation of Sound Propagation in Lined Ducts with Sheared Flows," *AIAA Journal*, Vol. 38, No. 5, 2001, pp. 768–773.

[7] Fung, K.-Y., Ju, H. B., and Tallapragada, B., "Impedance and Its Time-Domain Extensions," *AIAA Journal*, Vol. 38, No. 1, 2000, pp. 30–38.

[8] Fung, K.-Y., and Ju, H. B., "Broadband Time-Domain Impedance Models," *AIAA Journal*, Vol. 39, No. 8, 2001, pp. 1449–1454.

[9] Li, X. D., Richter, C., and Thiele, F., "Time-Domain Impedance Boundary Conditions for Subsonic Mean Flow," *Journal of the Acoustical Society of America*, Vol. 119, No. 5, May 2006, pp. 2665–2676.

[10] Rienstra, S. W., "Impedance Models in Time Domain, Including the Extended Helmholtz Resonator Model," AIAA Paper 2006-2686, May 2006.

[11] Chevaugeon, N., Remacle, J.-F., and Gallez, X., "Discontinous Galerkin Implementation of the Extended Helmholtz Resonator Model in Time Domain," AIAA Paper 2006-2569, May 2006.

[12] Richter, C., Thiele, F., Li, X., and Zhuang, M., "Comparison of Time–Domain Impedance Boundary Conditions by Lined Duct Flows," AIAA Paper 2006-2527, May 2006.

[13] Rienstra, S. W., and Eversman, W., "A Numerical Comparison Between the Multiple-Scale and Finite-Element Solution for Sound Propagation in Lined Flow Ducts," *Journal of Fluid Mechanics*, Vol. 437, June 2001, pp. 367–384.

[14] Jones, M. G., Watson, W. R., and Parrott, T. L., "Benchmark Data for Evaluation of Aeroacoustic Propagation Codes with Grazing Flow," AIAA Paper 2005-2853, May 2005.

[15] Watson, W. R., Jones, M. G., and Parrott, T. L., "A Quasi-3-D Theory for Impedance Eduction in Uniform Grazing Flow," AIAA Paper 2005-2848, May 2005.

[16] Li, X., Schemel, C., Michel, U., and Thiele, F., "Azimuthal Sound Mode Propagation in Axisymmetric Flow Ducts," *AIAA Journal*, Vol. 42, No. 10, Oct. 2004, pp. 2019–2027.

[17] Tam, C. K. W., and Webb, C., "Dispersion-Relation-Preserving Finite Difference Schemes for Computational Aeroacoustics," *Journal of Computational Physics*, Vol. 107, No. 2, Aug. 1993, pp. 262–281.

[18] Hu, F. Q., Hussaini, M. Y., and Manthey, J. L., "Low-Dissipation and Low-Dispersion Runge-Kutta Schemes for Computational Acoustics," *Journal of Computational Physics*, Vol. 124, No. 1, March 1996, pp. 177–191.

[19] Stanescu, D., and Habashi, W., "2N-Storage Low-Dissipation and Low-Dispersion Runge-Kutta Schemes for Computational Aeroacoustics," *Journal of Computational Physics*, Vol. 143, No. 2, July 1998, pp. 674–681.

[20] Richter, C., Panek, L., and Thiele, F., "On the Application of CAA-Methods for the Simulation of Indirect Combustion Noise," AIAA Paper 2005-2919, May 2005.

[21] Hu, F., "A Stable Perfectly Matched Layer for Linearized Euler Equations in Unsplit Physical Variables," *Journal of Computational Physics*, Vol. 173, No. 2, Nov. 2001, pp. 455–480.

[22] Tam, C., and Dong, Z., "Wall Boundary Conditions for High-Order Finite Difference Schemes in Computional Aeroacoustics," *Theoretical and Computational Fluid Dynamics*, Vol. 6, No. 6, 1994, pp. 303–322.

[23] Tam, C. K. W., Webb, C., and Dong, T. Z., "A Study of Short Wave

Components in Computational Aeroacoustics," *Journal of Computational Acoustics*, Vol. 1, March 1993, pp. 1–30.
[24] Zhuang, M., "Time Domain Impedance Boundary Conditions for a Slip Mean Flow Boundary," *Proceedings in Applied Mathematics and Mechanics*, Vol. 4, No. 1, 2004, pp. 530–531.
[25] Özyörük, Y., Long, L. N., and Jones, M. G., "Time-Domain Numerical Simulation of a Flow-Impedance Tube," *Journal of Computational Physics*, Vol. 146, No. 1, Oct. 1998, pp. 29–57.
[26] Li, X., Schemel, C., Michel, U., and Thiele, F., "On the Azimuthal Mode Propagation in Axisymmetric Duct Flows," AIAA Paper 2002-2521, June 2002.

X. Zhong
Associate Editor